Journal of Physics D:
Applied Physics

PAPER

2D modelling of key species dynamics in nanosecond pulsed N_2–H_2 plasma

To cite this article: Guobin Yang *et al* 2025 *J. Phys. D: Appl. Phys.* **58** 475202

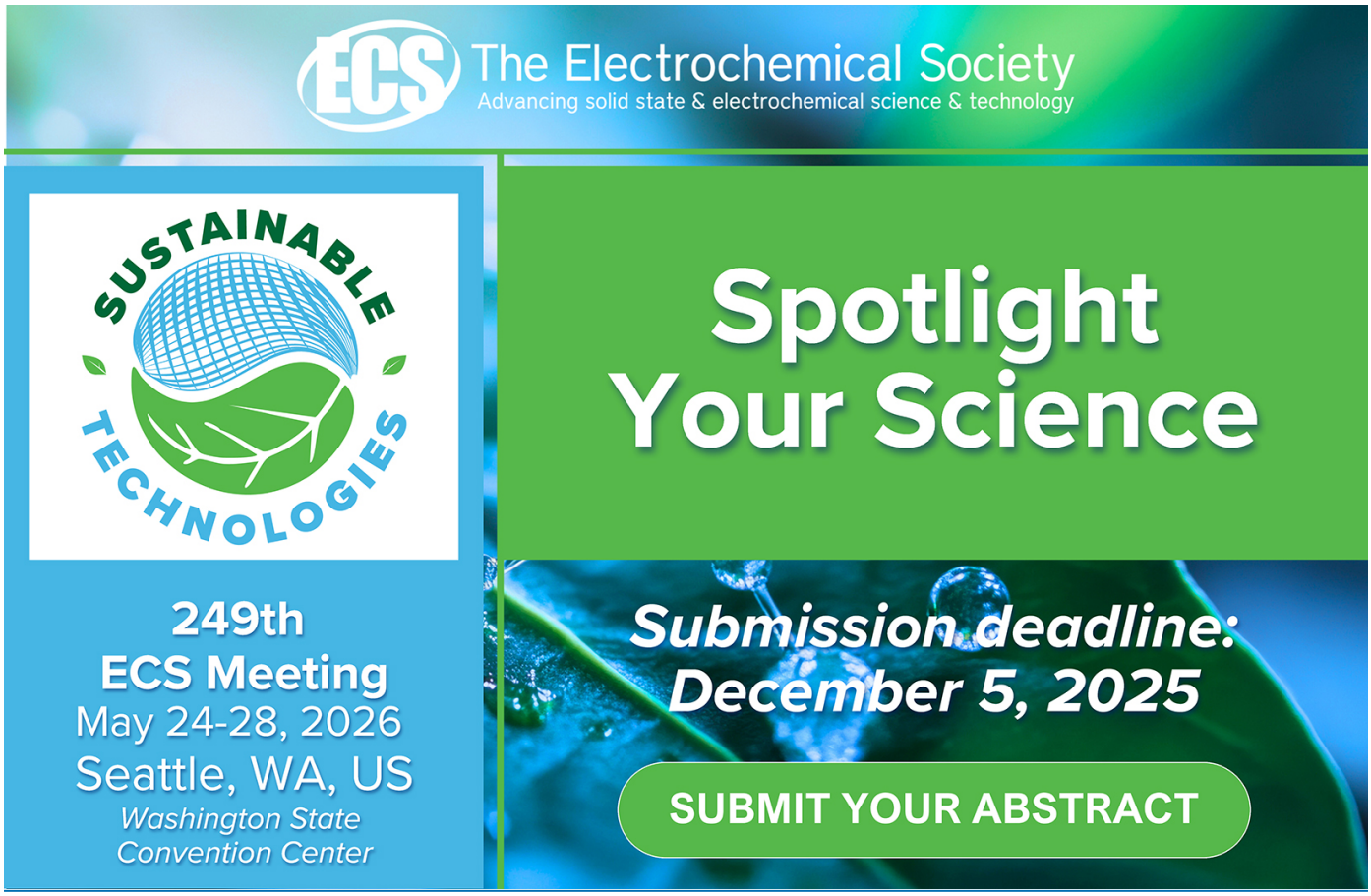

IOP Publishing Journal of Physics D: Applied Physics
J. Phys. D: Appl. Phys. **58** (2025) 475202 (16pp) https://doi.org/10.1088/1361-6463/ae1d87

2D modelling of key species dynamics in nanosecond pulsed N_2–H_2 plasma

Guobin Yang, She Chen*, Mengbo Li, Linlin Liu, Lipeng Zhong, Qiuqin Sun and Feng Wang

College of Electrical and Information Engineering, Hunan University, Changsha 410082, People's Republic of China

E-mail: chenshe@hnu.edu.cn

Received 4 August 2025, revised 24 October 2025
Accepted for publication 10 November 2025
Published 19 November 2025

Abstract

Low-temperature plasma-catalyzed ammonia synthesis is an environmentally friendly process well-suited for distributed energy systems. Among these methods, nanosecond pulsed discharge plasma is favored for its rapid production of reactive species that drive chemical reactions. However, prior studies were constrained by experimental limitations: key reactive species were difficult to measure, their behavior during the discharge process was poorly understood. Besides, zero-dimensional kinetic models overlooked the spatial distributions of species, electron energies, and electric fields. In this study, the spatiotemporal evolution of key reactive species in a plasma-assisted ammonia synthesis system is investigated. A two-dimensional fluid model is developed for ammonia synthesis under nanosecond pulsed voltage. A coaxial dielectric barrier discharge reactor with packed catalysts is employed to study the behavior of key species under varying peak voltages (v_p), pulse rise times (t_r), and catalyst dielectric constants (ε_r). The results indicate that plasma propagation inside the reactor occurs via surface ionization waves and filamentary micro-discharges. At $v_p = -10$ kV and $\varepsilon_r = 9$, the average densities of electrons, $N_2(v_1)$, $H_2(v_1)$, N, and H first rose and then fell with pulse rise time, peaking at 20 ns. At $t_r = 10$ ns and $\varepsilon_r = 9$, the average densities of all species increased with peak voltage. At $t_r = 10$ ns and $v_p = -10$ kV, electron, N, and H densities peaked at $\varepsilon_r = 15$, while $N_2(v_1)$ and $H_2(v_1)$ increased monotonically with dielectric constant. The model provides a theoretical basis to enhance ammonia synthesis in low-temperature plasma.

Supplementary material for this article is available online

Keywords: plasma, ammonia synthesis, nanosecond pulse, fluid model, dielectric barrier discharge

1. Introduction

Global energy and environmental challenges highlight the need for low-carbon and sustainable energy development [1]. Ammonia (NH_3) is not only one of the most widely used industrial chemicals worldwide but also a promising long-term energy carrier and an efficient zero-carbon fuel [2]. Currently, industrial ammonia production still relies on the conventional Haber–Bosch process, which requires nitrogen (N_2) and hydrogen (H_2) to react under high temperatures (650–750 K) and pressures (50–200 bar). This process accounts for 1%–2% of global energy consumption and contributes approximately 1.44% of global carbon dioxide (CO_2) emissions annually [3]. Therefore, there is an urgent need to develop alternative, sustainable, and environmentally friendly methods for ammonia synthesis.

Low-temperature plasma enables ambient ammonia synthesis through energetic electrons, excited molecules, ions, and radicals [4]. This reduces energy costs and enhances

* Author to whom any correspondence should be addressed.

production capacity. Dielectric barrier discharge (DBD) is one of the most widely used plasma sources [5], and can be generated using DC, AC, or pulsed power supplies [6]. Pulsed power supplies are highly favored for efficiently producing energetic electrons while keeping gas temperatures low [7]. Nanosecond pulsed discharge has been demonstrated to offer significant advantages in reducing discharge energy consumption and enhancing discharge uniformity. Zhang *et al* [8] reported that in atmospheric-pressure plasma characterization experiments, nanosecond pulsed discharges consumed approximately 1/13 the energy of sinusoidal AC discharges. Chen *et al* [9] experimentally demonstrated that increasing the pulse rise time from 50 ns to 500 ns improves discharge uniformity. Additionally, nanosecond pulsed plasma has been proven effective in improving the reaction performance of plasma-assisted ammonia synthesis. Kim *et al* [10] reported that pulsed power improved energy efficiency in Ru-catalyzed atmospheric-pressure plasma ammonia synthesis by a factor of four over AC power. Wang *et al* [11] achieved efficient ammonia synthesis using nanosecond pulsed plasma with only nitrogen and pure water under ambient temperature and pressure. Yang *et al* [12] reported that combining nanosecond pulsed and radio-frequency (RF) discharges, with a superimposed sub-breakdown RF waveform, enhanced the ammonia yield by 20%. Xu *et al* [13] employed nanosecond pulsed DBD for ammonia synthesis and achieved an ammonia synthesis rate of 5145.16 μmol·g^{-1}·h^{-1} and an efficiency of 0.48% under optimized conditions. Liu *et al* [14] found that shorter pulse rise times increase peak reduced electric field (E/N), elevate electron energy, and thus enhance N_2/H_2 activation and ammonia production. Kang *et al* [15] reported a similar finding. However, the maximum NH_3 volume fraction was observed at a pulse rising edge of 100 ns with a nitrogen-to-hydrogen ratio of 2:1. However, despite the ability to visualize enhanced ammonia synthesis performance, key parameters—such as electron density, electric field strength, electron temperature, and reactive species—remain difficult to measure directly during the reaction. For example, Cui *et al* [16] measured the electric field in a negative DC corona discharge via electric field-induced second harmonic generation, with the 1.5 mm laser–surface distance limiting accuracy. Chen *et al* [17] measured electron density in nanosecond pulse DBD using incoherent Thomson scattering, however, its low detection limit limited the detection of early-stage changes.

Many researchers have developed microkinetic models to elucidate the key reactions and intermediates in N_2–H_2 plasma ammonia synthesis [18]. Hong *et al* [19] conducted zero-dimensional modeling of atmospheric N_2–H_2 plasma, finding that radical–vibrational reactions are crucial and surface H(s) atoms dominate NH_3 formation. Van't Veer *et al* [20] used ZDPlasKin to develop a zero-dimensional plasma model, finding that filamentary microdischarges decompose NH_3, whereas the afterglow phase enhances its formation. Moreover, Van't Veer *et al* [21] developed another zero-dimensional kinetic model to study vibrational dynamics in DBD ammonia synthesis with and without packed beds. Their results indicate that microdischarges and uniform plasma both contribute to NH_3 production, vibrationally excited states accelerate N_2 dissociation, and the packing dielectric constant influences the electric field distribution, producing filamentary and surface discharges. Wang *et al* [22] studied streamer propagation in packed-bed DBD reactors with fillers of different dielectric constants using a fluid model and ICCD imaging. Higher dielectric constants shifted the discharge from surface to filamentary microdischarges, accelerated streamer propagation, and enhanced reactive species production, while reducing ozone due to increased high-energy electrons and N_2–O_2 ionization. Sun *et al* [18] reported from a zero-dimensional kinetic model that excited species N(^{2}D), $H_2(v_1)$, and $N_2(v)$ are critical for the formation of NH, NH_2, and N(s). However, zero-dimensional models often fail to capture the spatial distribution of key species within the reactor. Chen *et al* [23] developed a one-dimensional hydrodynamic model for plasma-catalyzed ammonia synthesis, mapping electric field, electron temperature, and density, and evaluating voltage, N_2:H_2 ratio, and catalyst site effects on NH_3 yield, providing a basis for two-dimensional extension. Zhang *et al* [24] used a 2D axisymmetric fluid model to study N_2/H_2 streamer development, finding that higher H_2 ratios enhance arc quenching and thermal breakdown resistance. Overall, direct observation of variations in electron density, electric field, and key reactive species during the process remains challenging. Moreover, most existing kinetic models for low-temperature plasma-catalyzed ammonia synthesis remain limited to zero- or one-dimensional. These models primarily focus on the evolution of key reactions and species during the discharge process and the identification of critical intermediates. However, they lack spatial resolution of relevant parameters, particularly under varying power supply conditions. Although one-dimensional plasma ammonia synthesis models can represent spatial distributions of parameters such as electron density and electric field strength to some extent, a significant gap remains between these models and the actual reactor structure.

In low-temperature atmospheric-pressure plasmas, low-electron energy plays a crucial role in breaking the N ≡ N triple bond and in generating reaction intermediates. This is primarily due to the long lifetimes of vibrationally excited molecules, which store significant energy [25]. In this context, vibrationally excited $N_2(v)$ can directly participate in N_2 dissociative adsorption. This occurs through two V–V energy transfer pathways: (1) transferring energy to H_2 to generate vibrationally excited $H_2(v)$ via $N_2(v_i-1)+H_2(v_j+1) \leftrightarrow N_2(v_i)+H_2(v_j)$; and (2) producing higher-energy $N_2(v)$ levels through $N_2(v_i-1)+N_2(v_j+1) \leftrightarrow N_2(v_i)+N_2(v_j)$. NH_x has been identified as a key intermediate in low-temperature plasma ammonia synthesis. According to literature [26], the reaction $H_2(v)+N \rightarrow NH+H$ is the dominant pathway for NH formation. Therefore, analyzing the spatial and temporal evolution of $N_2(v)$ and $H_2(v)$ during the reaction is essential. In addition, Atomic N and H drive NH formation in the gas phase and generate N(s) and H(s) via Eley–Rideal and Langmuir–Hinshelwood

surface reactions, playing a central role in ammonia synthesis. Thus, the spatial and temporal evolution of atomic N and H under varying reaction conditions warrants further investigation.

To investigate the mechanism of plasma-assisted ammonia synthesis, this study develops a two-dimensional fluid model of a simplified N_2–H_2 packed-bed reactor. The model examines the spatiotemporal distributions of electron density, reduced electric field strength, and key species, including first vibrational states of nitrogen $N_2(v_1)$ and hydrogen $H_2(v_1)$, as well as atomic nitrogen (N) and atomic hydrogen (H). The variations in these parameters offer valuable insights into optimizing reaction conditions for nanosecond pulsed plasma-catalyzed ammonia synthesis.

2. Model description

2.1. Plasma chemistry

The model includes 57 species and 64 chemical reactions. Reactions with long timescales are excluded, as this study focuses on nanosecond-scale plasma dynamics. The species and reaction pathways included in the model are listed in tables 1 and S1. These include electrons, ground-state molecules, positive and negative ions, atoms, and molecules in electronically or vibrationally excited states. This study focuses on the nanosecond-scale processes occurring within the reactor, mainly analyzing gas-phase species that are likely to trigger subsequent key surface or gas-phase reactions, while excluding plasma–catalyst surface interactions. It is mainly due to that most important surface reactions typically occur over a much longer timescale. Based on the literature [26], the gas-phase reaction mechanisms incorporated in the model include: (1) electron excitation and ionization, (2) vibrational excitation, (3) electron-impact dissociation, (4) dissociative ionization and recombination by electrons, and (5) ion–molecule reactions. The key species and reactions considered in this study (indicated by yellow arrows), along with the possible subsequent reactions (indicated by gray arrows), are shown in figure 1.

2.2. Governing equations for plasma dynamics

Plasma hydrodynamics is modeled by coupling the Poisson equation, the particle continuity equation, and the electron energy conservation equation [27]. Equation (1), the Poisson equation, determines the electric potential φ and electric field E distribution. Equation (2), the particle continuity equation, computes particle densities. Equation (3), based on the drift-diffusion approximation, describes particle transport. Finally, equation (4) calculates electron temperature using the conservation of electron energy. Following [24], the initial electron density is set to 1×10^{15} m^{-3} to simplify the influence of photoionization on streamer propagation.

$$E = -\nabla\varphi, \quad \nabla^2\varphi = -\frac{\rho}{\varepsilon_0} \tag{1}$$

$$\frac{\partial n_k}{\partial t} + \nabla \cdot G_k = S_k, \quad k = 1,2,\ldots,k_g \tag{2}$$

$$G_k = -\mu_k n_k \nabla\varphi - D_k \nabla n_k, \quad k = 1,2,\ldots,k_g \tag{3}$$

$$\begin{aligned}\frac{\partial \varepsilon_e}{\partial t} + \nabla \cdot \left(\tfrac{5}{3}\varepsilon \boldsymbol{G}_e - \tfrac{5}{3} n_e D_e \nabla\varepsilon\right) = &+ e\boldsymbol{G}_e \cdot \nabla\phi \\ -e\sum_i \Delta E_i^e r_i - &\tfrac{3}{2} k_b n_e \tfrac{2m_e}{m_{kb}} (T_e - T_g)\, \nu_{e,kb}\end{aligned} \tag{4}$$

Here, E denotes the electric field, φ is the electric potential, ρ represents the space charge density, and ε_0 is the vacuum permittivity. G_k represents the flux of species k, and S_k is the source term accounting for the production and loss of that species. n_k, μ_k, and D_k represent the density, mobility, and diffusion coefficient of species k, respectively [28]. The total electron energy is approximated by the average electron energy, given as $\varepsilon_e \approx (3/2)\, n_e k_B T_e$. The three source terms on the right-hand side of equation (4) represent Joule heating, inelastic collision heating, and elastic collision heating, respectively. e is electron unit charge, the energy lost by an electron in a single collision event is ΔE_i, which involves a reaction i with r_i, the rate of progress, and ν_k denotes the momentum transfer collision frequency for the species. T_e and T_g represent the electron temperature and gas temperature, respectively. The local field approximation is employed to relate particle transport coefficients to the reduced electric field, using results obtained from Bolsig+ calculations. In the two-dimensional model, the gas temperature is fixed at 300 K, and the pressure is maintained at 1 atm, with a nitrogen-to-hydrogen ratio of 3:1.

2.3. Reactor configuration and parameter settings

This study employs the passkey parallel streamer solver with kinetics, based on the finite element method, to simultaneously resolve multiple coupled physical equations. The computational grid spacing is 10 μm in both X and Y directions. The time step is adaptively determined based on the Courant–Friedrichs–Lewy condition, medium relaxation time, and reaction kinetics timescales. Figure 2 presents a two-dimensional cross-sectional schematic of the reactor geometry. The reactor comprises two coaxial quartz tubes, each 0.5 mm thick, with $\varepsilon_r = 9$. The inner electrodes were connected to a pulsed power supply with a pulse width of 50 ns. The external electrodes were grounded, and the radial discharge gap was maintained at 3 mm. Catalyst beads with a radius of 0.9 mm were uniformly packed in the discharge gap and directly contacted one another, which is same as the experiment setup of [29].

3. Result and discussion

3.1. Discharge dynamics inside the reactor

Figures 3 and 4 present the temporal evolution of electron density and electric field distributions within the reactor, for $t_r = 10$ ns, $v_p = -10$ kV, and catalyst $\varepsilon_r = 9$. As observed in previous studies [30], the plasma develops via filamentary micro-discharges and surface ionization wave discharges

Table 1. Chemical species considered in the model.

Types	Species
Ground-state and vibrationally excited molecules	$N_2(X)$,$H_2(X)$,$N_2(X,v_i)$ $1 \leqslant i \leqslant 8$, $H_2(X,v_i)$ $1 \leqslant i \leqslant 3$,
Electronically excited molecules	N_2(A3,B3,W3,C3,E3,a1,w1,a2),H_2(B3,B1,C3,A3,C1,G1,D3)
Ions	N_2^+,N_4^+,H_2^+,N^+,H^+,H^-,NH_3^+,NH_3^-
Atoms and NHx particles	N,N(2P,4P,4S,4D),H,H(2P,2S,1,2,3),NH_3,NH_2,NH_3(V2,V4,V13,e1,e2)

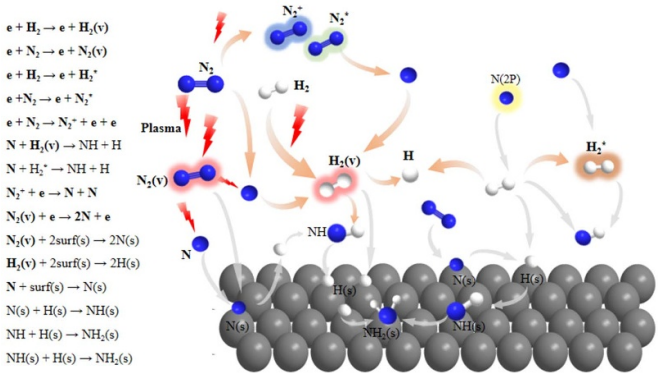

Figure 1. Key reactions and subsequent processes involving $N_2(v)$, $H_2(v)$, N, and H species.

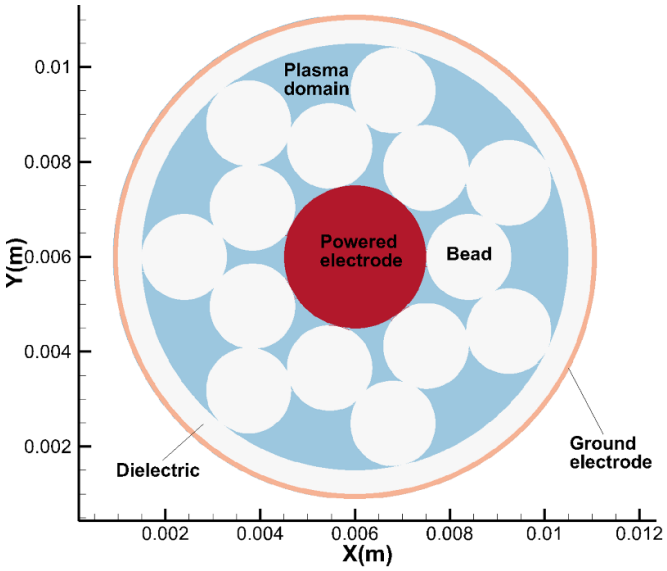

Figure 2. Simulation geometry.

inside the reactor. Figure 4(a) illustrates that the intense electric field (E/N ≈ 250 Td) between the inner electrode and the adjacent catalyst bead induces strong electron collision reactions. These reactions produce high-energy electrons, leading to the formation of a high-energy electron density region with an average electron density of about 4.29×10^{19} m^{-3}, as illustrated in figure 3(a). Under the influence of the surface electric field (E/N ≈ 200 Td) in figure 4(b), a surface discharge propagates along the catalyst, as shown in figure 3(b). When the discharge approaches the inner surface adjacent to the outer catalyst bead, the polarized electric field between the inner and outer beads reaches about 228 Td, thereby further intensifying the discharge [31]. This leads to the formation of negative streamers, reaching electron densities of approximately 2×10^{19} m^{-3} at 13 ns. Subsequently, surface discharges propagate along both sides of the inner surface of the outer beads. As shown in figures 3(c) and (d), the discharge in the outer void region is mainly confined to the surface due to the distorted electric field induced by space charge accumulation, with the near-surface E/N reaching about 272 Td, which

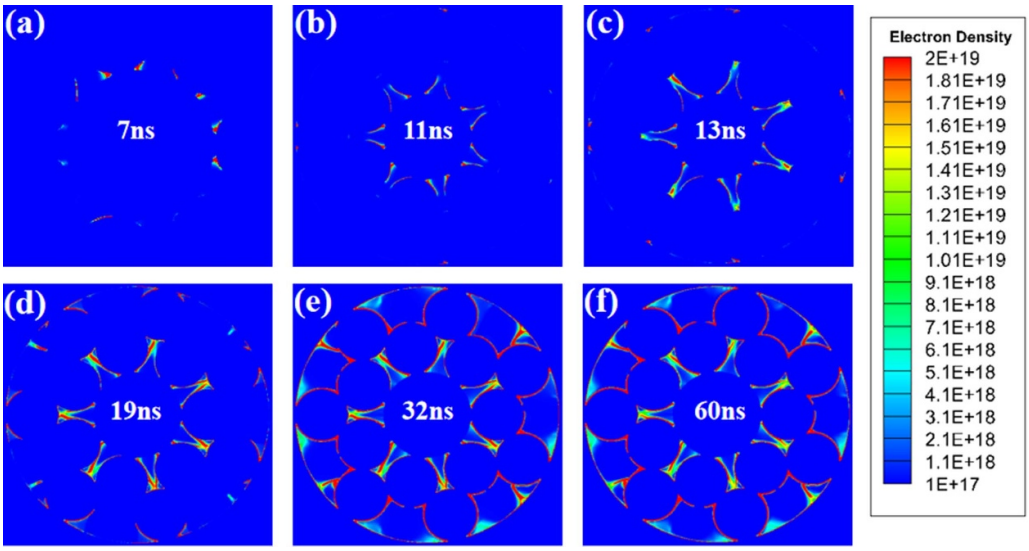

Figure 3. Evolution of electron density at $t_r = 10$ ns, $v_p = -10$ kV, and catalyst $\varepsilon_r = 9$. (a) 7 ns; (b) 11 ns; (c) 13 ns; (d) 19 ns; (e) 32 ns; (f) 60 ns.

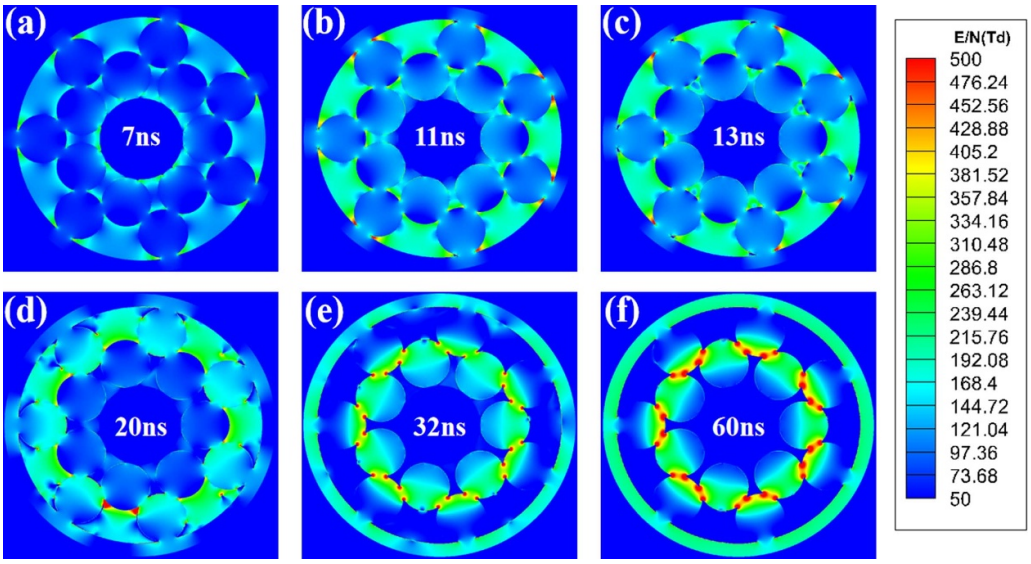

Figure 4. Evolution of the reduced electric field at $t_r = 10$ ns, $v_p = -10$ kV, and catalyst $\varepsilon_r = 9$. (a) 7 ns; (b) 11 ns; (c) 13 ns; (d) 20 ns; (e) 32 ns; (f) 60 ns.

is considerably higher than that in the gap center. In certain regions, however, the distorted electric field induces the formation of positive streamers along the surface of the dielectric layer, directed toward the catalyst beads. This phenomenon is consistent with the observations reported by Zhang *et al* [32]. At 32 ns, as shown in figures 3(d) and 4(d), the discharge becomes relatively stable, exhibiting an average electron density of approximately 4.8×10^{19} m^{-3}, and maintains this stability until 60 ns. Notably, the maximum electron density consistently appears on the surface of the catalyst beads, providing a reliable driving force for surface reactions that are likely to occur in practice.

3.2. Influence of pulse voltage parameters on plasma dynamics

3.2.1. Effect of pulse rise time on discharge characteristics. In this section, we examine how varying pulse rise times influence plasma behavior, with $v_p = -10$ kV and catalyst $\varepsilon_r = 9$. Figures 5 and 6 show that shorter pulse rise times yield higher discharge currents and increased energy delivery [33]. Figure 5 further indicates that the peak electron density at a 10 ns rise time is 5.93×10^{21} m^{-3}, compared to 5.43×10^{21} m^{-3} at 40 ns, demonstrating that shorter rise times produce higher peak electron densities. However, figure 7(a)

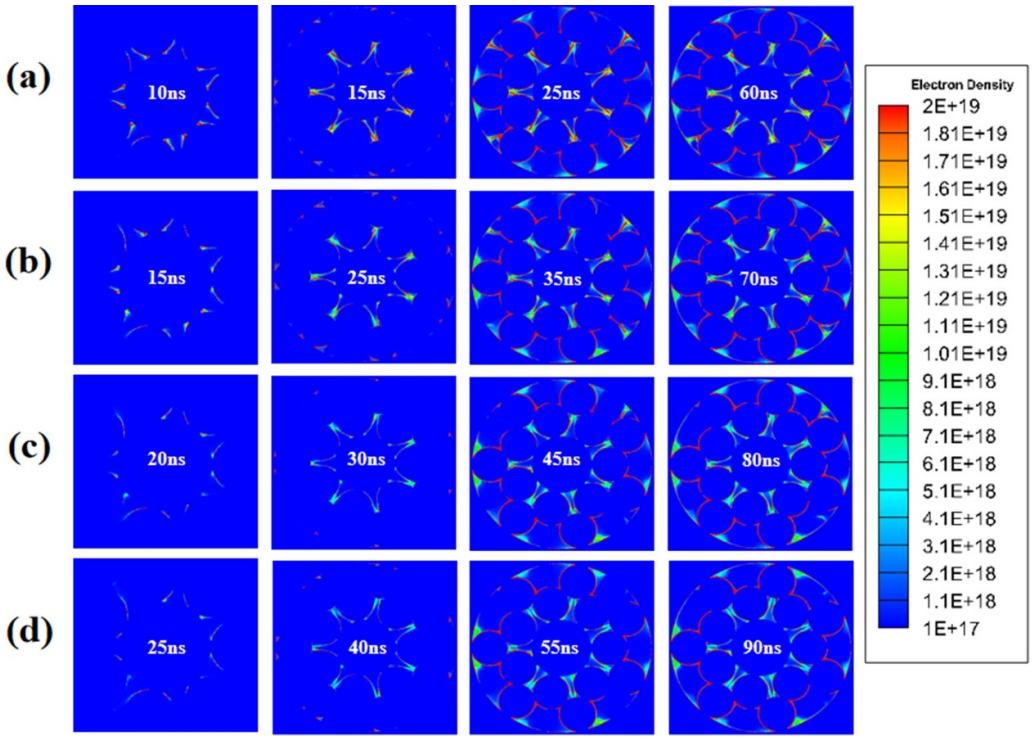

Figure 5. Evolution of electron density for different pulse rise times at $v_{\mathrm{p}} = -10$ kV and catalyst $= 9$. (a) 10 ns; (b) 20 ns; (c) 30 ns; (d) 40 ns.

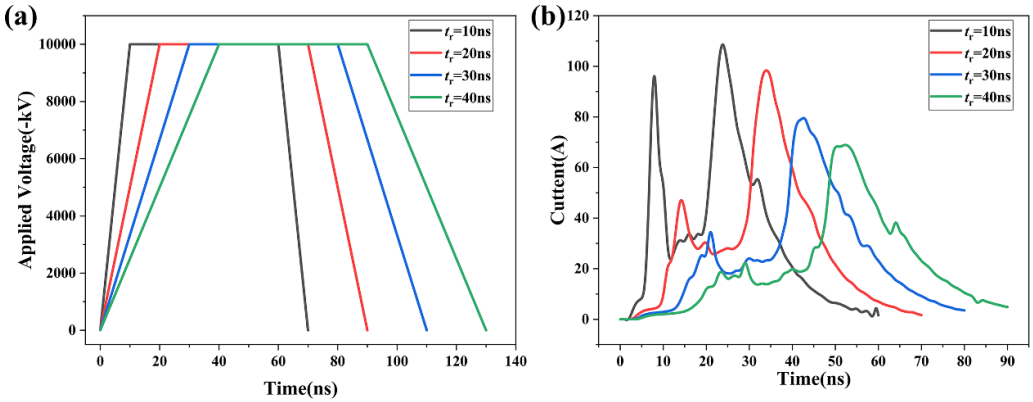

Figure 6. Waveforms of (a) voltage and (b) current with varying rise times.

shows that after discharge stabilization, the highest average electron density occurs at $t_{\mathrm{r}} = 20$ ns. At this point, the electron density distribution is more uniform, which likely contributes to improved ammonia synthesis efficiency, as reported in recent studies [34]. At shorter rise times, the rapid increase in electric field strength initiates intense electron avalanches, resulting in partial discharges characterized by exponential increases in electron density. This explains why the highest peak electron density and discharge current occur at 10 ns. In contrast, a longer pulse rise time leads to a slower rate of change in electric field strength, resulting in lower average electron energy (figure 7(b)) and weaker ionization. This may account for the disappearance of the outer gap streamer observed in figure 5. In contrast, at $t_{\mathrm{r}} = 20$ ns, the electric field strength increases quickly but not excessively. Electron avalanches develop moderately while allowing sufficient diffusion. This yields the most homogeneous spatial electron distribution and highest average electron density—supporting previous findings that excessively steep rise edges hinder plasma homogeneity [9].

Reactions E16 and E39 require only 0.3 eV and 0.52 eV of energy input, respectively, resulting in much higher densities of $N_2(v_1)$ and $H_2(v_1)$ compared to ions, radicals, or electronically excited species. As shown in figures 8(a),(b) and 9, the average densities of $N_2(v_1)$ and $H_2(v_1)$ peak at a 20 ns rise time, reaching 9.19×10^{21} m^{-3} and 2.04×10^{21} m^{-3}, respectively. This indicates that $N_2(v_1)$ and $H_2(v_1)$ are more uniformly distributed at 20 ns, consistent with the distribution pattern

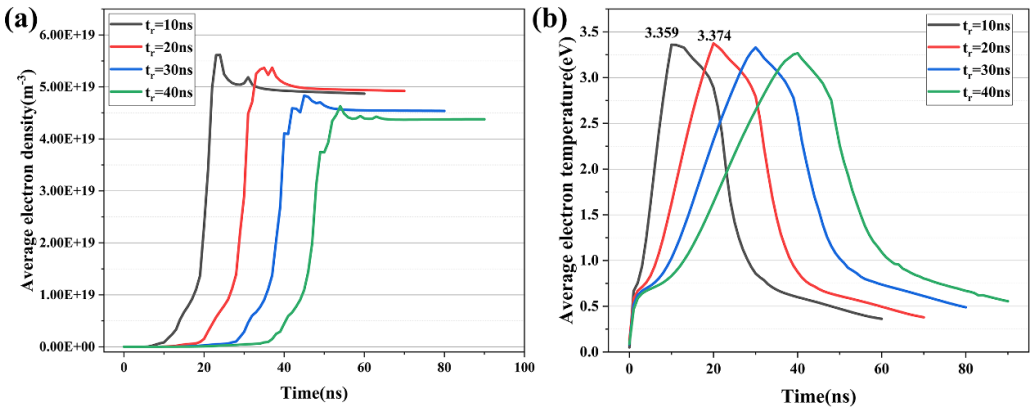

Figure 7. Variation of (a) average electron density and (b) average electron temperature over time under different rise time conditions.

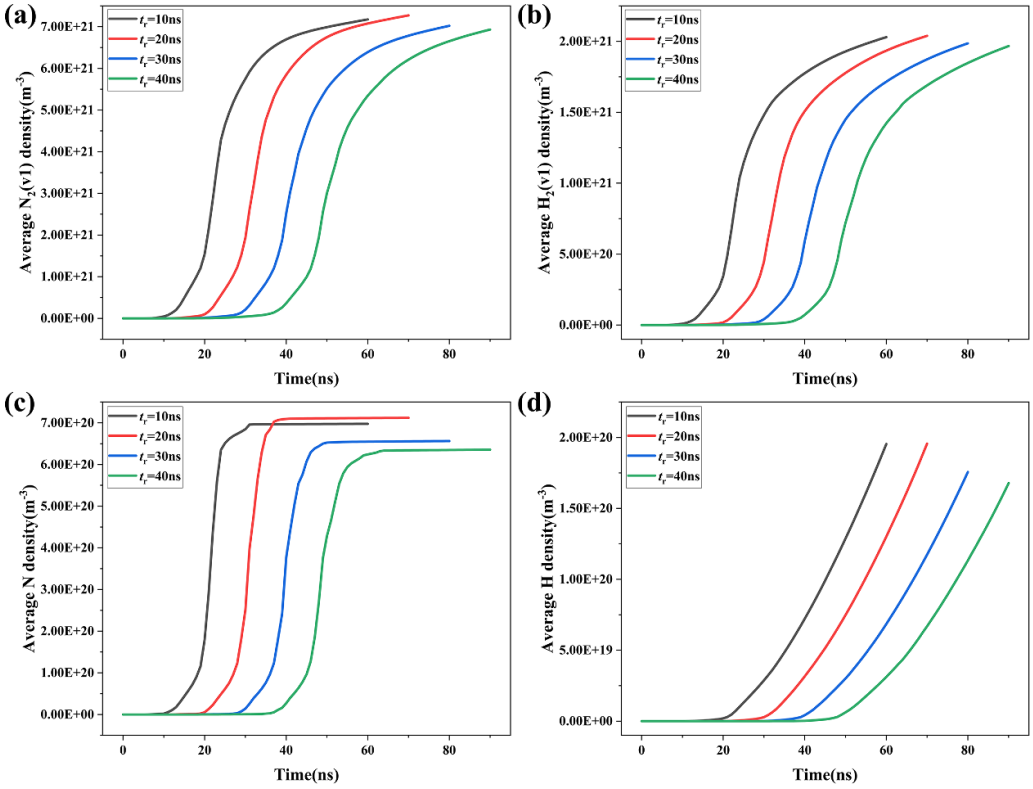

Figure 8. Variation of the average densities of (a) $N_2(v_1)$, (b) $H_2(v_1)$, (c) N, and (d) H over time under different rise time conditions, at $v_p = -10$ kV and catalyst $\varepsilon_r = 9$.

of average electron density. This may be because shorter rise times rapidly increase the electric field strength, accelerating electrons to high energies more quickly. As a result, more electrons undergo ionization rather than vibrational excitation. In contrast, longer rise times lead to slower rise of electric field. Electrons then lose energy through inelastic collisions, shifting the energy distribution toward lower values (figure 7(b)). At $t_r = 20$ ns, as previously described, the moderately increasing electric field strength neither causes excessive electron energy loss nor directs a large portion of electrons toward ionization. Consequently, both the average electron density (figure 7(a)) and the average electron energy (figure 7(b)) reach higher values. This indicates that more electrons are available for vibrational excitation of N_2 and H_2, resulting in the highest average densities of $N_2(v_1)$ and $H_2(v_1)$ at this time. The peak $H_2(v_1)$ density is approximately one order of magnitude lower than that of $N_2(v_1)$, due to the 3:1 nitrogen-to-hydrogen ratio in the model and the higher energy requirement for $H_2(v_1)$ excitation compared to $N_2(v_1)$.

Figure 10 shows the spatial distributions of N and H densities at the onset of the pulse voltage decline under different rise times. From figures 8(c) and (d) and 10, it is observed that the maximum average densities of atomic N and H are 7.12×10^{20} m^{-3} and 1.96×10^{20} m^{-3},

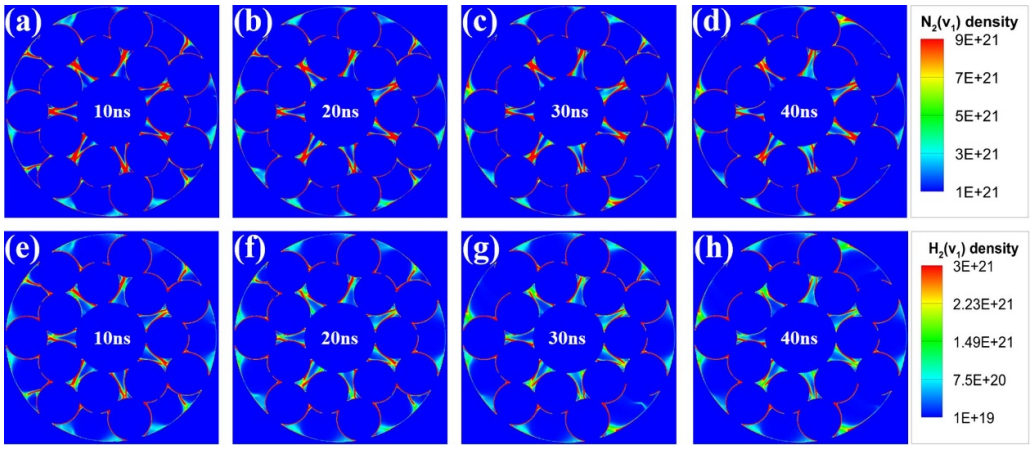

Figure 9. Densities of (a)–(d) $N_2(v_1)$ and (e)–(h) $H_2(v_1)$ at the initiation of the falling edge of the pulse under $v_p = -10$ kV, catalyst $\varepsilon_r = 9$, and varying rise times.

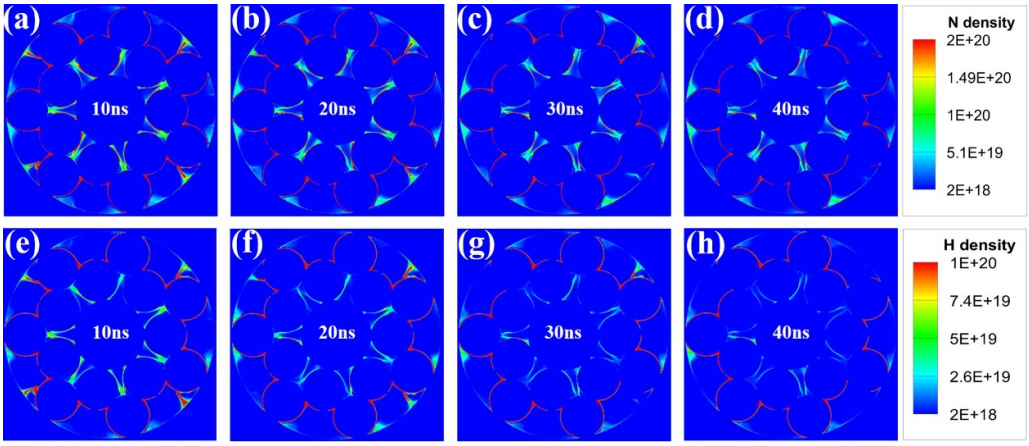

Figure 10. Densities of (a)–(d) N and (e)–(h) H at the initiation of the falling edge of the pulse under $v_p = -10$ kV, catalyst $\varepsilon_r = 9$, and varying rise times.

respectively. Both maxima occur at $t_r = 20$ ns, consistent with the trends of vibrational species and electron density. This result aligns with previous analysis: at $t_r = 20$ ns, sufficient high-energy electrons are available to drive dissociation reactions (E14 and E64), while maintaining good spatial homogeneity, leading to the highest average densities of N and H atoms.

3.2.2. Effect of peak voltage on discharge characteristics. This section examines the impact of varying peak voltages on discharge characteristics, with $t_r = 10$ ns and catalyst $\varepsilon_r = 9$. Figure 11 illustrates that both discharge current and power increase with rising peak voltage. Figure 12 and S1 show that higher peak voltages generate stronger reduced electric fields and more intense electron collision reactions. This results in increased average electron density within the reactor void and enhanced overall discharge uniformity, facilitating more streamer channels between catalyst beads and the surrounding medium in both inner and outer reactor regions. Furthermore, figure 12 indicates that higher peak voltages accelerate discharge development. Notably, figure 13 shows that the average electron temperature reaches its peak at $v_p = -10$ kV after 13 ns. This phenomenon may be attributed to the rapid ionization rate at high peak voltages, producing more electrons and accumulating surface charge on catalyst beads. This creates a stronger reverse electric field, which slows electron acceleration and reduces electron energy. Moreover, the slope of the waveform in figure 13(b) suggests that although electron temperature initially rises rapidly at higher voltages, increased collisions with gas molecules transfer energy more quickly to heavy particles, causing a rapid electron temperature decline.

Based on figures 14–16, increasing the peak voltage to -14 kV yields significant increases in reactive species densities: $H_2(v_1)$ rises to 2.97×10^{21} m^{-3}, $N_2(v_1)$ to 1.09×10^{22} m^{-3}, atomic N to 8.91×10^{20} m^{-3}, and atomic

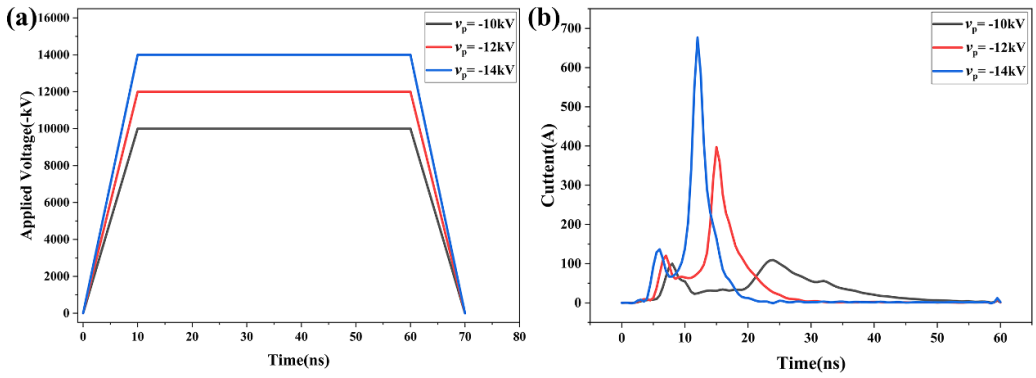

Figure 11. Waveforms of (a) voltage and (b) current with varying peak voltage.

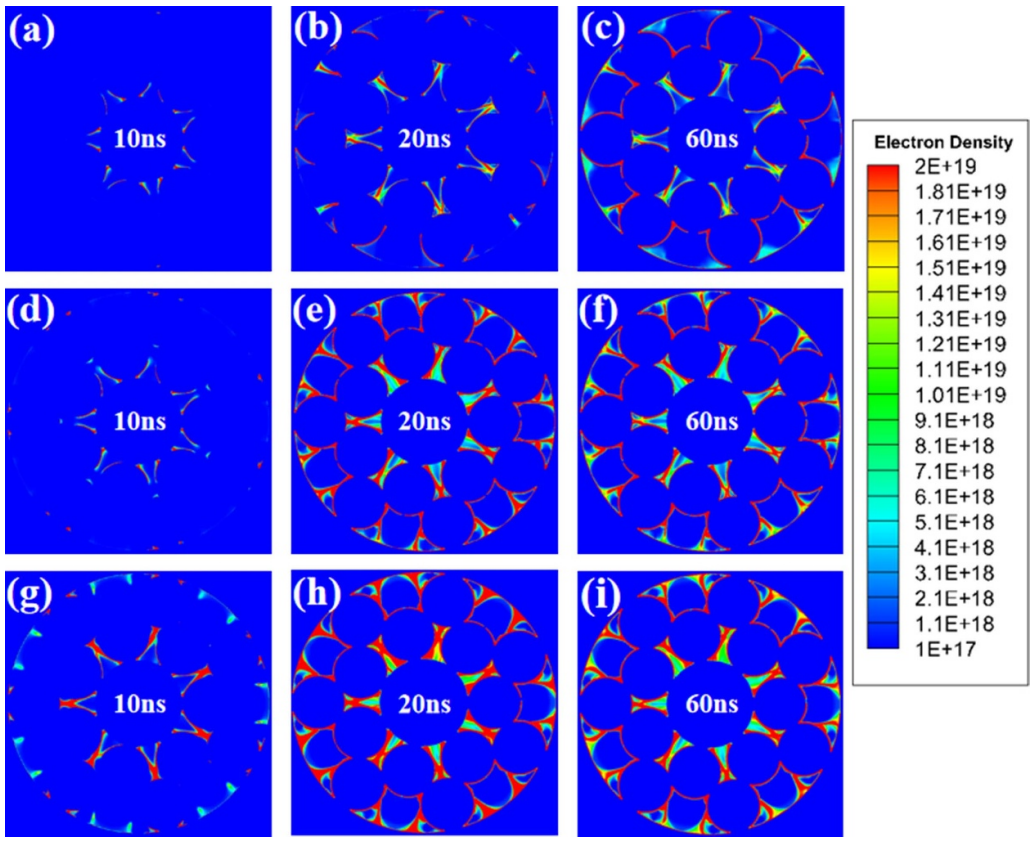

Figure 12. Evolution of electron density with $t_r = 10$ ns and catalyst $\varepsilon_r = 9$, at voltage peaks of (a)–(c)−10 kV, (d)–(f)−12 kV, and (g)–(i)−14 kV, respectively.

H to 4.31 × 10^2 m^{-3}—each showing notable improvements compared to the −10 kV case. This increase is attributable to the higher electric field intensity achieved in the reactor for the same duration, which promotes a more uniform discharge and enhances the density of reactive species. However, it was demonstrated that excessively high voltages accelerate NH_3 decomposition and reduce overall energy yield due to increased discharge power, indicating the existence of an optimal operating voltage [3, 35–37].

3.3. Effect of catalyst dielectric constant on discharge characteristics

This section discusses the influence of catalyst dielectric constants on discharge characteristics, under $t_r = 10$ ns and $v_p = -10$ kV. As shown in figures 17, 18, and S2, increasing the catalyst dielectric constant enhances the local electric field within 22 ns, resulting in faster discharge development and higher average electron density. As the discharge progresses, the average electron density slightly decreases.

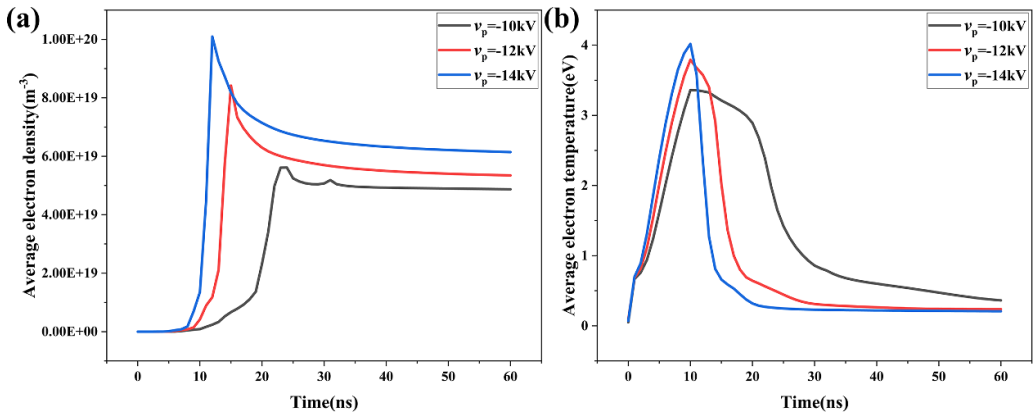

Figure 13. Average (a) electron density and (b) electron temperature at different time points, with $t_r = 10$ ns, catalyst $\varepsilon_r = 9$, and $v_p = -10$ kV,-12 kV, and -14 kV, respectively.

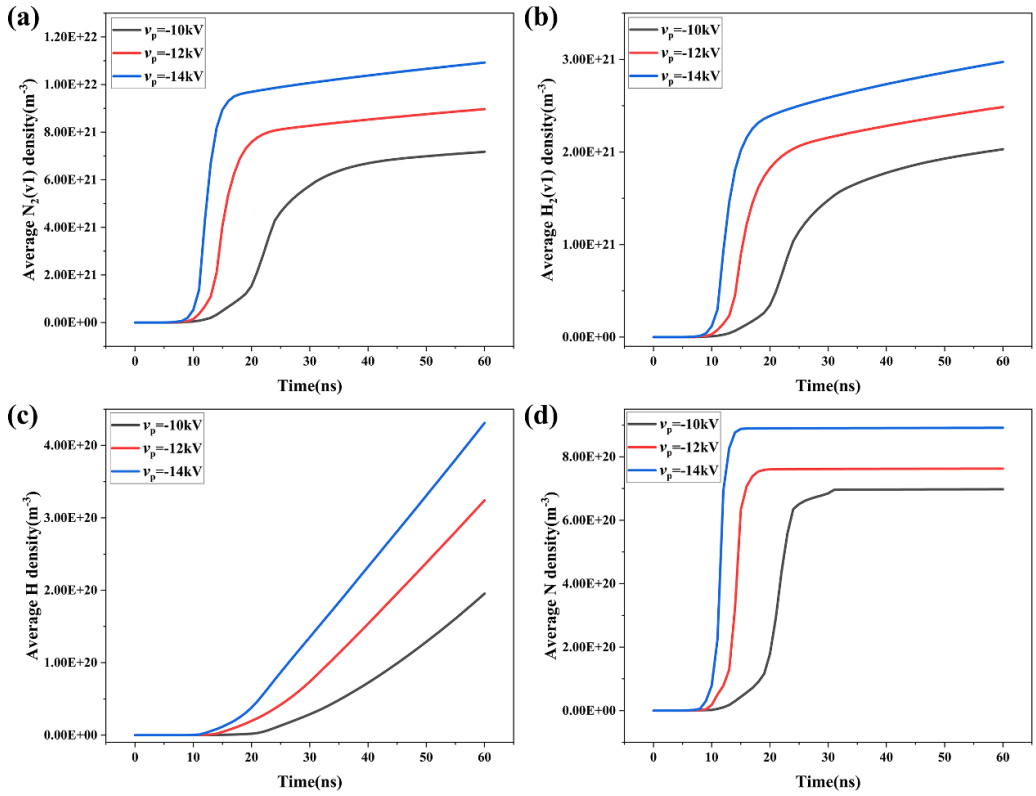

Figure 14. Average densities of (a) $N_2(v_1)$, (b) $H_2(v_1)$, (c) H, and (d) N at different times, with $t_r = 10$ ns, catalyst $\varepsilon_r = 9$, and $v_p = -10$ kV,-12 kV, and-14 kV, respectively.

At 60 ns, the reactor exhibits average electron densities of 4.87×10^{19} m^{-3} for $\varepsilon_r = 9$, 5.61×10^{19} m^{-3} for $\varepsilon_r = 15$, and 5.48×10^{19} m^{-3} for $\varepsilon_r = 25$, indicating a general trend of initial increase followed by a slight decline.

According to Maxwell–Wagner interfacial polarization theory, at discharge initiation, increasing the dielectric constant enhances inter-particle and particle-dielectric polarization. This intensifies the local electric field, as shown in figure S2. The stronger electric field (figure 18) increases electron energy. Consequently, ionization, dissociation, and vibrational excitation reactions are enhanced. This accelerates discharge development and yields higher, more uniformly distributed electron densities. However, as streamer continues, a higher dielectric constant may cause surface charge accumulation on catalyst beads, which in turn generates an electric field opposing the original field and weakens the effective reduced

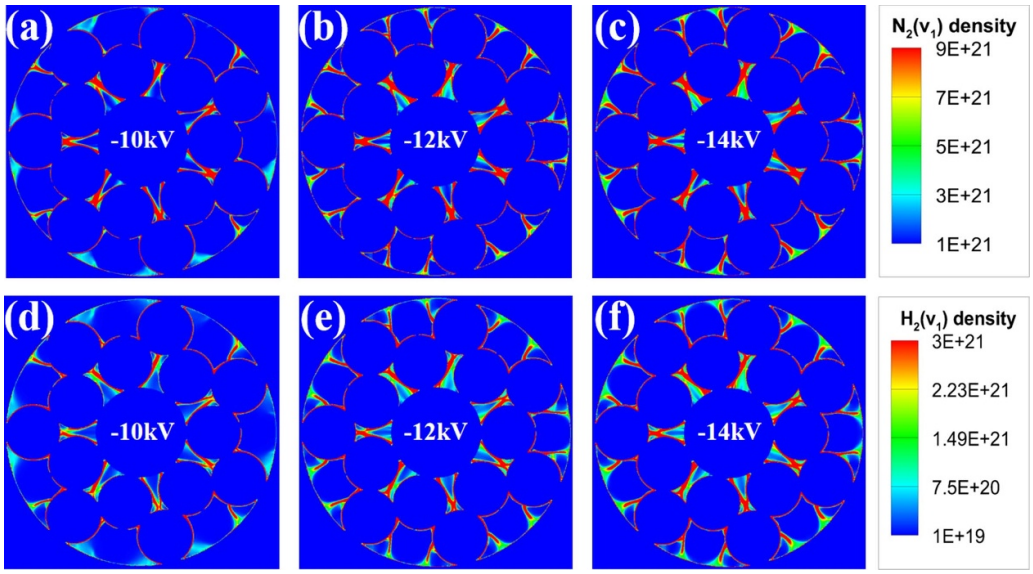

Figure 15. Densities of (a)–(c) $N_2(v_1)$ and (d)–(f) $H_2(v_1)$ at the initiation of the falling edge of the pulse, for $t_r = 10$ ns, catalyst $\varepsilon_r = 9$, and $v_p = -10$ kV, -12 kV, and-14 kV, respectively.

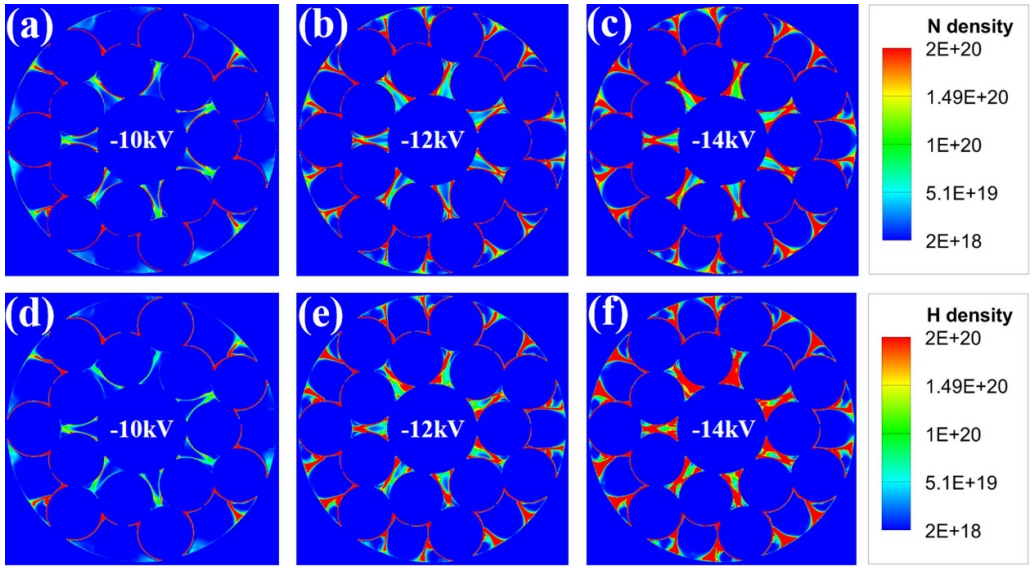

Figure 16. Densities of (a)–(c) N and (d)–(f) H at the initiation of the falling edge of the pulse, for $t_r = 10$ ns, catalyst $\varepsilon_r = 9$, and $v_p = -10$ kV,-12 kV, and -14 kV, respectively.

electric field intensity. This effect is shown in figure S2. The local field strength near catalyst contact points decreases during streamer propagation at higher dielectric constants, for example, at 20 ns, the reduced electric field at a specific point on the catalyst bead increases from 316 Td ($\varepsilon_r = 9$) to 351 Td ($\varepsilon_r = 15$), and then sharply drops to 58 Td ($\varepsilon_r = 25$). At $\varepsilon_r = 15$, the electric field is strong enough to support a stable discharge without substantial weakening caused by surface charge, resulting in the highest average electron density. Figures 19–21 reveal that average densities of $N_2(v_1)$ and $H_2(v_1)$ increase monotonically with dielectric constant. In contrast, N and H densities follow the same trend as the average electron density. This difference arises because N and H are produced primarily via high-energy electron–induced dissociation (E14 and E64). The trend in average electron energy and density (figure 18) reflects the high-energy electron population. At $\varepsilon_r = 15$, the reactor contains the most high-energy electrons, yielding maximum N and H densities (8.14×10^{20} m^{-3} and 2×10^{20} m^{-3}). By contrast, $N_2(v_1)$ and $H_2(v_1)$ have low vibrational excitation thresholds and can be efficiently excited by low-energy electrons. As a result, a decrease in average electron energy has little impact on their populations. Therefore, $N_2(v_1)$ and $H_2(v_1)$ exhibit different trends compared to N and H radicals.

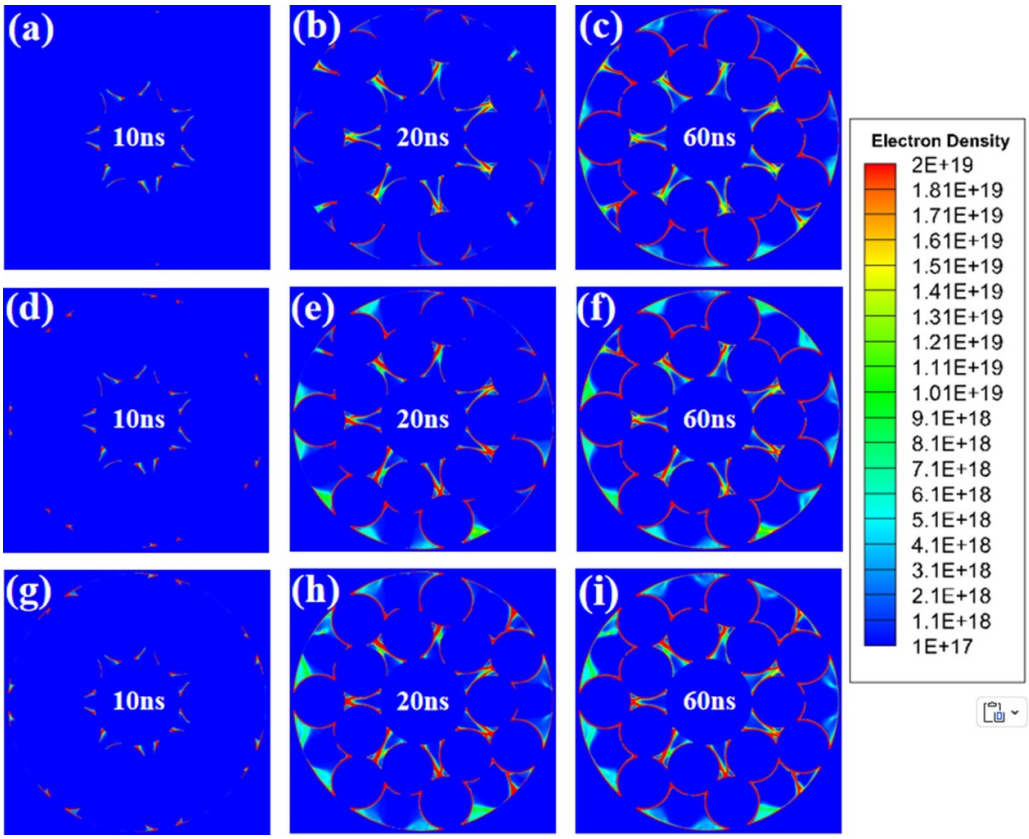

Figure 17. Evolution of electron density at $t_r = 10$ ns and $v_p = -10$ kV for catalysts with dielectric constants of (a)–(c) 9, (d)–(f) 15, and (g)–(i) 25.

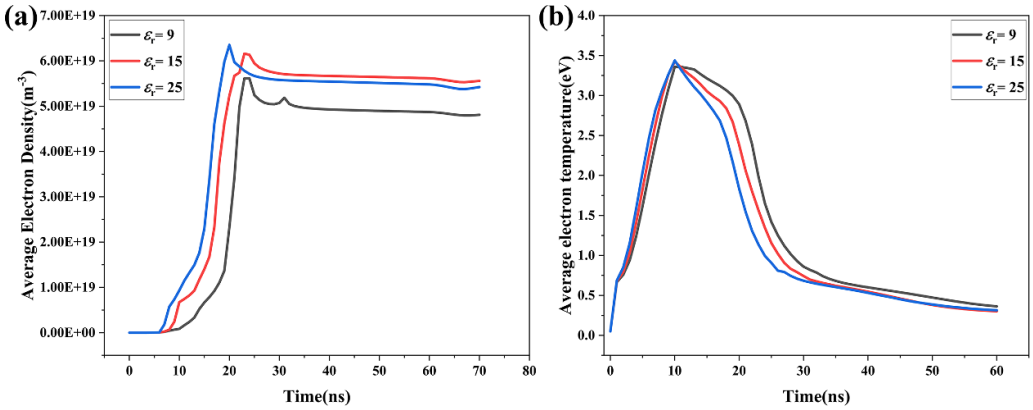

Figure 18. (a) Average electron density and (b) mean electron temperature at different times, for $t_r = 10$ ns, $v_p = -10$ kV, and catalyst $\varepsilon_r = 9$, 15, and 25, respectively.

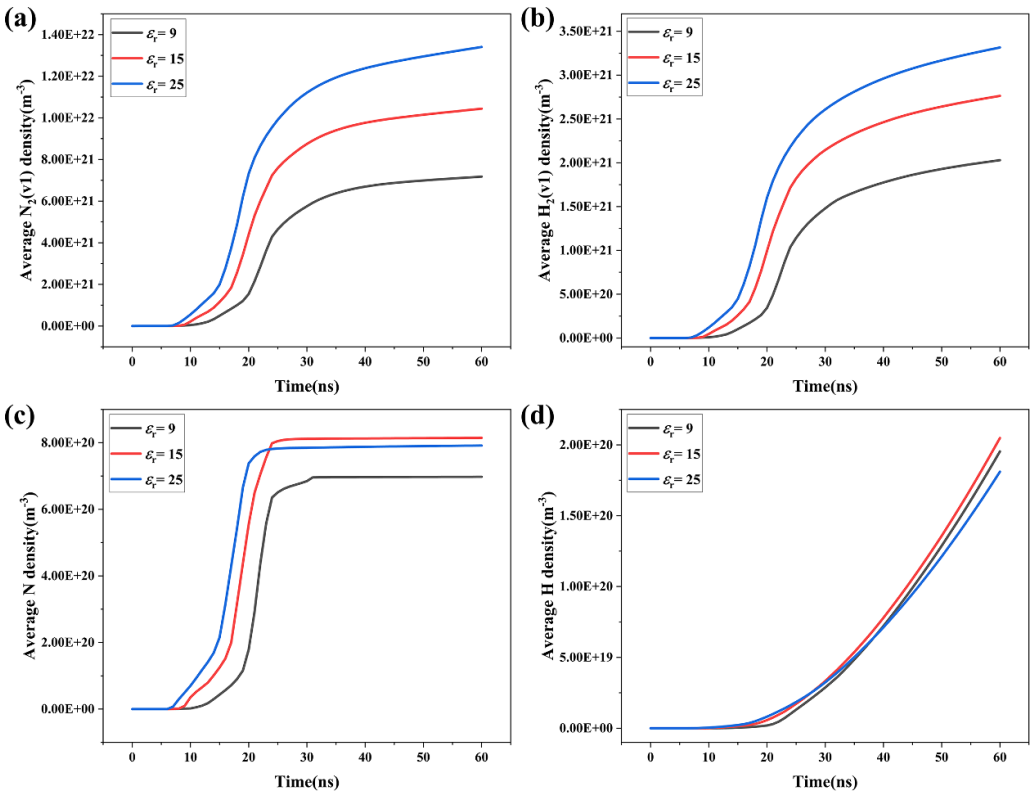

Figure 19. Average densities of (a) $N_2(v_1)$, (b) $H_2(v_1)$, (c) N, and (d) H at different times, for $t_r = 10$ ns, $v_p = -10$ kV, and catalyst $\varepsilon_r = 9$, 15, and 25, respectively.

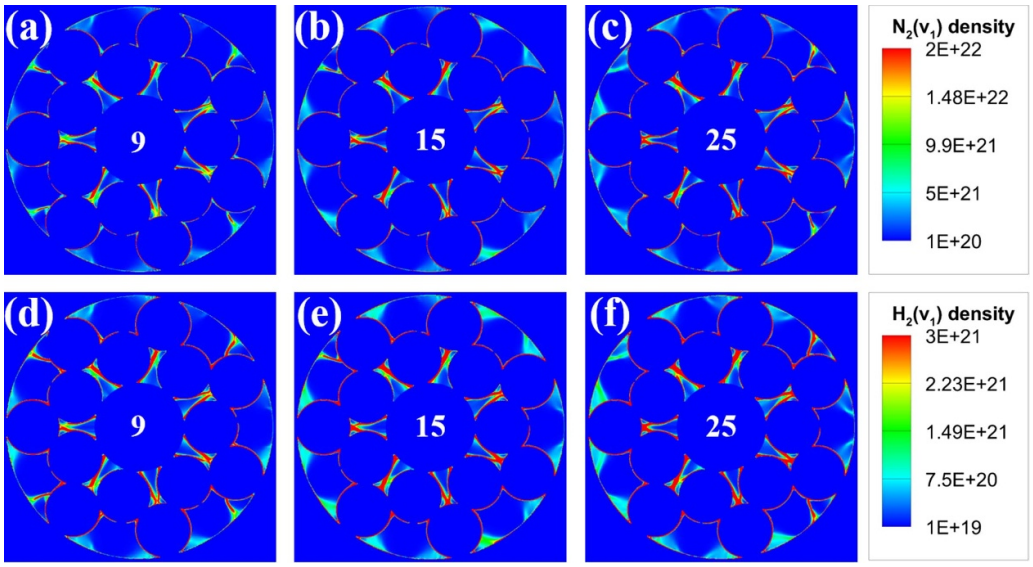

Figure 20. Densities of (a)–(c) $N_2(v_1)$ and (d)–(f) $H_2(v_1)$ at initiation of the falling edge of the pulse, for $t_r = 10$ ns, $v_p = -10$ kV, and catalyst $\varepsilon_r = 9$, 15, and 25, respectively.

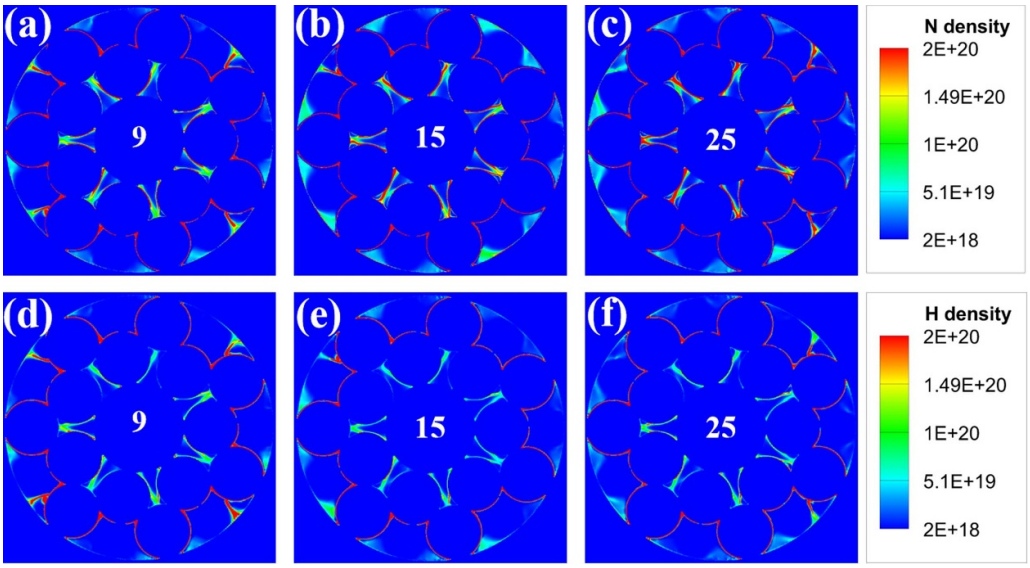

Figure 21. Densities of (a)–(c) N and (d)–(f) H at initiation of the falling edge of the pulse, for $t_r = 10$ ns, $v_p = -10$ kV, and catalyst $\varepsilon_r = 9$, 15, and 25, respectively.

4. Conclusion

This study presents a 2D fluid model for ammonia synthesis under nanosecond pulsed voltage. The model investigates streamer discharge dynamics and the spatiotemporal evolution of key N_2 and H_2 species at 0.1 MPa and 300 K, under varying pulse parameters and catalyst dielectric constants.

The results indicate that the discharge initially occurs in the high electric-field region at the interface between the electrode and the catalyst bead. Subsequently, the plasma evolves into surface ionization waves and filamentary microdischarges. Throughout the process, the maximum electron density consistently appears on the catalyst surface, highlighting the critical role of surface reactions in low-temperature plasma-assisted ammonia synthesis.

In addition, a shorter pulse rise time leads to a stronger discharge current. With increasing rise time, the peak electron density decreases, whereas the average electron density initially increases and then decreases, reaching a maximum of 4.92×10^{19} m^{-3} at a rise time of 20 ns. The average densities of key species—including $N_2(v_1)$, $H_2(v_1)$, atomic N, and atomic H—follow a trend similar to that of the average electron density. This behavior may be attributed to the fact that, at $t_r = 20$ ns, the electric field strength rises moderately, enabling moderate electron avalanche development and providing adequate time for diffusion. The average electron temperature reaches its maximum at this point, enhancing the vibrational excitation and dissociation reactions. Furthermore, increasing the peak pulse voltage strengthens the overall discharge intensity, resulting in higher average electron density and elevated average densities of various reactive species.

The maximum average electron density of 5.61×10^{19} m^{-3} is observed at a dielectric constant of 15, as the dielectric constant increases from 9 to 25. This enhancement is attributed to the stronger surface electric field at higher dielectric constants, which accelerates electrons, increases the ionization rate, and consequently raises the electron density. However, as the dielectric constant continues to increase, a stronger reverse electric field is generated, suppressing the discharge and thereby reducing the electron density. Since the generation of N and H primarily depends on dissociative collisions with high-energy electrons, their average densities follow the same trend as the electron density. In contrast, due to their low excitation thresholds, $N_2(v_1)$ and $H_2(v_1)$ are less affected by the decrease in average electron energy. As a result, the average densities of $N_2(v_1)$ and $H_2(v_1)$ increase with dielectric constant.

This study is limited by the exclusion of plasma–catalyst surface interactions and the assumption of idealized reactor conditions, so further experimental validation and more comprehensive multi-physics modeling are required. In future work, we will further investigate optimal pulse parameters through experimental validation, with a particular focus on discharge characteristics and species evolution driven by the synergistic interactions between the plasma and the catalyst surface.

Data availability statement

All data that support the findings of this study are included within the article (and any supplementary files).

Supplementary data available at https://doi.org/10.1088/1361-6463/ae1d87/data1.

Acknowledgment

This work was supported by National Natural Science Foundation of China (Grant Nos. 52377143 and 52237007).

Conflict of interest

The authors declare that they have no known competing financial interests or personal relationships that could have appeared to influence the work reported in this paper.

Author contributions

Guobin Yang 0009-0003-3297-6665
Conceptualization (equal), Data curation (equal), Formal analysis (equal), Investigation (equal), Methodology (equal), Software (equal), Writing – original draft (equal), Writing – review & editing (equal)

She Chen 0000-0001-7013-1442
Conceptualization (equal), Formal analysis (equal), Funding acquisition (equal), Methodology (equal), Project administration (equal), Supervision (equal), Writing – review & editing (equal)

Mengbo Li
Conceptualization (equal), Data curation (equal), Formal analysis (equal), Methodology (equal)

Linlin Liu
Data curation (equal), Formal analysis (equal), Investigation (equal)

Lipeng Zhong 0000-0002-8435-7298
Data curation (equal), Formal analysis (equal), Investigation (equal)

Qiuqin Sun 0000-0003-0732-5126
Methodology (equal), Software (equal)

Feng Wang
Project administration (equal), Supervision (equal), Visualization (equal)

References

[1] Gharahshiran V S and Zheng Y 2024 Sustainable ammonia synthesis: an in-depth review of non-thermal plasma technologies *J. Energy Chem.* **96** 1–38
[2] Bogaerts A, Neyts E C, Guaitella O and Murphy A B 2022 Foundations of plasma catalysis for environmental applications *Plasma Sources Sci. Technol.* **31** 053002
[3] Wang Y, Yang W, Xu S, Zhao S, Chen G, Weidenkaff A, Hardacre C, Fan X, Huang J and Tu X 2022 Shielding protection by mesoporous catalysts for improving plasma-catalytic ambient ammonia synthesis *J. Am. Chem. Soc.* **144** 12020–31
[4] Tianyu L, Jing S and Yuting G 2024 Research progress on plasma catalysis and its applications in power-to-X *Trans. China Electrotech. Soc.* **39** 5461–81
[5] Xueting H, Yuan G and Liguang D 2022 Study on plasma enhanced CH_4-CH_3OH conversion to liquid chemicals by nanosecond pulsed dielectric barrier discharge *Trans. China Electrotech. Soc.* **37** 3941–50
[6] Ma J, Yu L, Yao C, Dong S, Li C, Ren L and Wang S 2024 10 kV nanosecond pulse generator with high voltage gain and reduced switches *High Volt.* **9** 1059–67
[7] Walsh J L and Kong M G 2007 10ns pulsed atmospheric air plasma for uniform treatment of polymeric surfaces *Appl. Phys. Lett.* **91** 251504
[8] Zhang S, Wang W, Jiang P, Yang D-Z, Jia L and Wang S 2013 Comparison of atmospheric air plasmas excited by high-voltage nanosecond pulsed discharge and sinusoidal alternating current discharge *J. Appl. Phys.* **114** 163301
[9] Chen J, Liang H and Wei B 2019 Discharge characteristics of surface dielectric barrier discharge driven by parameterized nanosecond pulsed power supply *High Volt. Eng.* **45** 3365–74
[10] Kim H-H, Teramoto Y, Ogata A, Takagi H and Nanba T 2017 Atmospheric-pressure nonthermal plasma synthesis of ammonia over ruthenium catalysts *Plasma Process. Polym.* **14** 1600157
[11] Wang Y, Wang Q, Sun S, Xin Y, Zhu X and Sun B 2023 Highly efficient ammonia synthesis by gas-liquid interface pulsed discharge plasma: a synthesis method without hydrogen *ACS Sustain. Chem. Eng.* **11** 13070–80
[12] Yang X, Richards C and Adamovich I V 2023 Ammonia generation in Ns pulse and Ns pulse/RF discharges over a catalytic surface *Plasma Sources Sci. Technol.* **32** 064003
[13] Xiaofang X U, Meng S U N and Qinlong S 2024 Dielectric barrier discharge plasma-assisted catalytic ammonia synthesis: synergistic effect of Ni-MOF-74 catalyst and nanosecond pulsed plasma *Plasma Sci. Technol.* **26** 064005
[14] Liu Y, Zhang H-B and Chen Q 2023 Optimization of process parameters for ammonia synthesis by nanosecond pulsed dielectric barrier discharge plasma *Chin. J. Appl. Chem.* **40** 268–76
[15] Shaofen K, Shuai Z and Xiaoxiao C 2021 Study on reduction of nitrogen to ammonia by nanosecond pulse dielectric barrier discharge plasma *High Volt. Eng.* **47** 368–75
[16] Cui Y, Zhuang C and Zeng R 2019 Electric field measurements under negative DC corona discharges in ambient air by electric field induced second harmonic generation *Appl. Phys. Lett.* **115** 244101–9
[17] Chen T, Goldberg B and Rousso A C 2020 Timeresolved measurements of electric field, electron temperature, and electron density in a nanosecondpulsed dielectric barrier discharge *AIAA Scitech 2020* (Forum) p 2148
[18] Sun J, Chen Q, Zhao X, Lin H and Qin W 2022 Kinetic investigation of plasma catalytic synthesis of ammonia: insights into the role of excited states and plasma-enhanced surface chemistry *Plasma Sources Sci. Technol.* **31** 094009
[19] Hong J, Pancheshnyi S, Tam E, Lowke J J, Prawer S and Murphy A B 2017 Kinetic modelling of NH_3 production in N_2–H_2 non-equilibrium atmospheric-pressure plasma catalysis *J. Phys. D: Appl. Phys.* **50** 154005
[20] Van't Veer K, Engelmann Y, Reniers F and Bogaerts A 2020 Plasma-catalytic ammonia synthesis in a DBD plasma: role of microdischarges and their afterglows *J. Phys. Chem. C* **124** 22871–83
[21] Van't Veer K, Reniers F and Bogaerts A 2020 Zero-dimensional modeling of unpacked and packed bed dielectric barrier discharges: the role of vibrational kinetics in ammonia synthesis *Plasma Sources Sci. Technol.* **29** 045020
[22] Wang W, Kim H-H, Van Laer K and Bogaerts A 2018 Streamer propagation in a packed bed plasma reactor for plasma catalysis applications *Chem. Eng. J.* **334** 2467–79
[23] She C, Hongmei L and Ting W 2021 1D fluid model of catalytic ammonia synthesis enhanced by low temperature plasma *Trans. China Electrotech. Soc.* **36** 2730–9

[24] Zhang R, Wang L, Liu J, Lian Z and Wang Z 2023 Numerical simulation of streamer development process in N_2/H_2 environment at elevated temperature *IEEE Trans. Plasma Sci.* **51** 1150–63
[25] Capitelli M, Ferreira C M and Gordiets B F 2013 *Plasma Kinetics in Atmospheric Gases* Springer Science & Business Media
[26] Hong J, Prawer S and Murphy A B 2018 Plasma catalysis as an alternative route for ammonia production: status, mechanisms, and prospects for progress *ACS Sustain. Chem. Eng.* **6** 15–31
[27] He J, Peng B, Yu G, Wang R, Jiang N, Li J and Wu Y 2024 Experimental and numerical study on atmospheric-pressure air dielectric barrier discharge via 50 Hz/5000 Hz dual-frequency excitation *High Volt.* **9** 391–402
[28] Cheng H, Li Y, Zheng K, Liu D and Lu X 2021 Numerical analysis of nitrogen fixation by nanosecond pulse plasma *J. Phys. D: Appl. Phys.* **54** 184003
[29] Cheng H, Ma M, Zhang Y, Liu D and Lu X 2020 The plasma enhanced surface reactions in a packed bed dielectric barrier discharge reactor *J. Phys. D: Appl. Phys.* **53** 144001
[30] Kruszelnicki J, Engeling K W, Foster J E, Xiong Z and Kushner M J 2016 Propagation of negative electrical discharges through 2-dimensional packed bed reactors *J. Phy. D* **50** 025203
[31] De La Hoz M, Pieterse P J and Etxegarai A 2024 Comparison of corona effect prediction criteria on sphere-plane configuration *High Volt.* **9** 957–69
[32] Zhang Y, Wang H, Jiang W and Bogaerts A 2015 Two-dimensional particle-in cell/Monte Carlo simulations of a packed-bed dielectric barrier discharge in air at atmospheric pressure *New J. Phys.* **17** 083056
[33] Li Y, Qin L, Yang D Z, Zhang L and Wang W C 2022 The effect of voltage pulse shape on the discharge characteristics in the packed bed reactor under air and nitrogen *Appl. Sci.* **12** 2215
[34] Lu K, Xu Y, Yuan H, Liang J, Wang H, Zhang J, Li Y and Yang D 2025 Non-thermal plasma synergistic Ni/Al_2O_3 for ammonia synthesis: configuration and optimization of a double dielectric barrier discharge reactor *Int. J. Hydrog. Energy* **97** 835–44
[35] Li K, Chen S, Li M, Liu L, Li Y and Wang F 2024 Plasma-catalyzed ammonia synthesis over $La(OH)_3$ catalyst: effects of basic sites, oxygen vacancies, and H_2 plasma treatment *Int. J. Hydrog. Energy* **59** 1287–96
[36] Li K, Chen S, Li M, Liu L, Li Y, Yang G and Wang F 2025 Enhancing ammonia synthesis efficiency with Ni-loaded La_2O_3 catalysts in plasma-catalyzed reactions *Plasma Process. Polym.* **22** 2400212
[37] Gorky F, Guthrie S R, Smoljan C S, Crawford J M, Carreon M A and Carreon M L 2021 Plasma ammonia synthesis over mesoporous silica SBA-15 *J. Phys. D: Appl. Phys.* **54** 264003